

Opti-Enc: On the Path to the Optimal Encoder-Decoder for Thermal Image Colorization for Cross Domain Colorized Images

Suranjan Goswami, IEEE Student Member

Satish Kumar Singh, Senior Member, IEEE

Abstract

Thermal images can be obtained as either grayscale images or pseudo colored images based on the thermal profile of the object being captured. In this work, we explore what an optimal encoder decoder might look like for creating a thermal-optical fused domain image. We compare the results from several different encoder-decoder structures with different networks to answer this question. This output images obtained from our method provides information of both domains jointly in a colorized image. We call this a cross domain colorized image. We also present a robust registration method for thermal and optical pairs, which can work despite changes in resolution and the make of the thermal imager. Lastly, we present a unique public dataset with registered thermal-visual image pairs containing around 1800 images as a part of this work, collected over a period of 2 years. We compare our results with prior literature, show how our results are different and discuss on some future work that can be explored further in this domain.

1. Introduction

Encoder Decoder structures which model data to be reduced to an optimal representation and then scale it up to a representative output, have emerged as one of the most popular deep learning techniques to handle any regression task in recent years. This can range from colorization [2], [34] to specialized information extraction [46-47] or even recognition [44], [48-49] amongst a host of other applications. The general rule of thumb applied to such models is to minimize patch size to the lowest possible level (down to 1) and then scale it up to the necessary resolution. The next level of optimization in these algorithms is to then add in a skip connection at each progressive level to concatenate the output from similar levels, finally obtaining the necessary output. This model is finally trained against a database of input to output images to obtain the necessary weights at each level. This seems like a very good generalization of most regression tasks as is evidently shown by the encouraging results obtained. However, with the ever increasing level of optimization and similar structures, one of the most important questions that arise is if this is indeed the most optimal way to design an encoder-decoder.

We try to look into this question and conduct extensive experiments to see what would happen if we were to use a database which instead of having fully similar data points (images in this case), used widely differing data points as a small percentage (around 4.5%) included in the training database. We conduct this experiment on the field of thermal image colorization and compare our results with a recent work which uses a similar architecture as we are using, but with the usual characteristics of encoder decoder structures like going down to a patch size of 1x1 along with skip connections. Our assumption of an optimal level in an encoder-decoder is in line with the work presented in [42] where the authors theorize that there is a minimal patch of image which is needed in order to recognize it. Thus, similarly, an encoder should have an optimal patch size before the results would start to degrade instead of improving. We proceed with our work based on this assumption and show that this is indeed a viable hypothesis.

Of course, in order to prove this we had to include a degree of dissimilar images as a part of the database. This is because if the images used in the experiment are all very similar to each other, even if the lowest level of patch used in an encoder-decoder structure goes down to 1, the optimal distribution would be maintained by virtue of the training points being very close to each other in the data space.

We choose to work in the domain of thermal imaging because based on the principle of emitted radiation, it is possible to capture images in complete darkness, as long as there is a temperature difference between the object being captured and the surrounding. It needs to be noted that when we are talking about infrared images, we specifically mean Thermal Infrared (TIR) images. TIR images are different from Near Infrared (NIR) in the sense that NIR images incorporate optical band information in an infrared image. NIR images are quite similar to optical domain images and seem to possess sharper edges as compared to TIR images, but they would not work in complete darkness because of the same reason. However, barring a few expensive thermal imagers, all of them work with a primary thermal imager and a secondary optical sensor.

The first problem with these imagers is that they are usually not centred at the same point on the 2 images. The shift is random, based on the distance of the object being captured, located from the

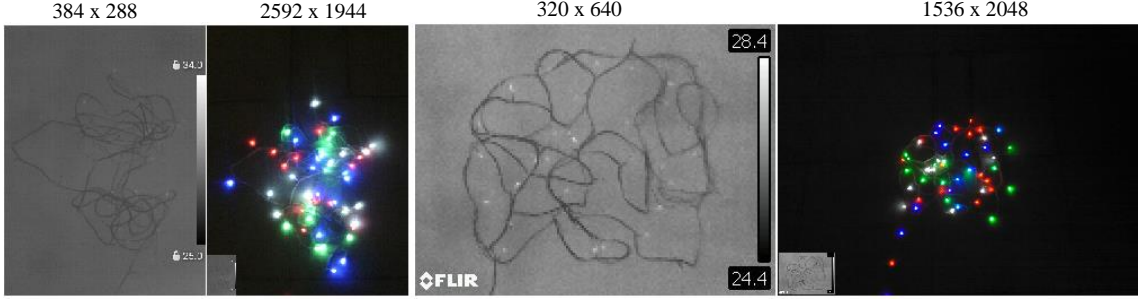


Figure 1: A comparison of the sizes of the thermal image vs the optical image for a scene captured via 2 different thermal imagers. Figure (a) is captured via Sonel KT400 and figure (b) is the image captured via FLIR E40. The thermal images for each are inset on the bottom left of the optical images for a visual comparison. The images on the left are the thermal images and those on the right are the optical images. These images were used to obtain the Homography constants for the rescaling factors of the images obtained via the thermal imagers

thermal imager. This is primarily because the thermal sensor and the optical sensor are physically located at different points in a general thermal imager. Here, we propose a registration technique, which works in order to obtain the optimal area of an optical image based on the corresponding thermal image. We also introduce an open access paired image dataset [32], with diverse images. The images that we are presenting comprise of images from a natural setting (greenery), modern setting (buildings), crowd setting and historical buildings. Although the number of paired images in this database are not very high (1843 pairs), the point we are trying to make here is that we have used 2 different thermal imagers (of 2 different makes, with different resolutions across the internal cameras) and varied subject settings while training our networks. Our technique works with the said constraints, proving that it is a robust method even under varying conditions.

The deep learning algorithm we create is used to obtain a color mask for a thermal prior. Once we have obtained this mask, we fuse it with the thermal image. This is done because our motivation was to preserve the information that is obtained in the thermal domain while producing a colorized image, rather than produce a purely optical colorized image. This is a big challenge because the TIR image data is different from optical images due to the difference in sensors being used. Moreover, the algorithm might provide different color outputs based on the thermal profile of the same scene, irrespective of the optical ground truth based on the illumination profile of the thermal data. For example, the same scene photographed during day and night would yield different optical images due to the difference in illumination, but provide the same thermal image as long as the relative surrounding temperature profile remains the same. Hence, we create a fusion technique which is able to preserve the characteristics present in a thermal image for better human perception. This is based on the idea that a human is more likely to notice the features in a colorized image rather than in a grayscale image. After all, color can provide more information than grayscale [1], especially in domains dealing

specifically with night vision problems like in surveillance and assistive driving, where perceptual information enhancement forms an important field. While traditional methods for image colorization have included techniques like scribble-based colorization [16], labelling [17], color transfer from images based on similarity matching [18-20] and feature extraction [21], newer methods based on Convolutional Neural Networks (CNN) are coming to the forefront at a very rapid speed. Grayscale to color image conversion [9], [22-25] is a very important topic in this field. While there have not been much work on thermal images in this aspect, Near Infrared Images, by virtue of their similarity to grayscale images have had some work [26-27], [14] presented as well. Other innovative uses for thermal images include its application in biometric security for identification with thermal based vein patterns [38] and pedestrian detection for safe driving [39], among others.

While there has been a research work by Berg et al. [2], on thermal image colorization, it specifically focuses on only one domain of images, namely images from vehicle traffic [3] from the KAIST Multispectral (MS) Pedestrian Dataset. This is also the case with the work by X Kuang et al. [4], who use a Generative Adversarial Network (GAN) to process images from the same database as [34], which uses stacked encoder-decoder for colorization. There have been multiple sources which have reported that GANs are difficult to train because finding the correct hyper parameters needed to tune the networks are quite difficult [5], [6], [7], [8]. However, this method becomes much easier when the images being used are from a single domain. Since we are trying to work on finding an optimal distribution for an encoder decoder structure for a varied database, we do not take the route of using GANs for our work. For the singular purpose of thermal image colorization, another avenue of work that could be considered is style transfer for images via GAN [28-30] for synthetic data preparation. A particular domain for this includes using CycleGAN [36] for creating realistic images for a single domain, like in the case of transforming facial TIR images into their visible counterparts as

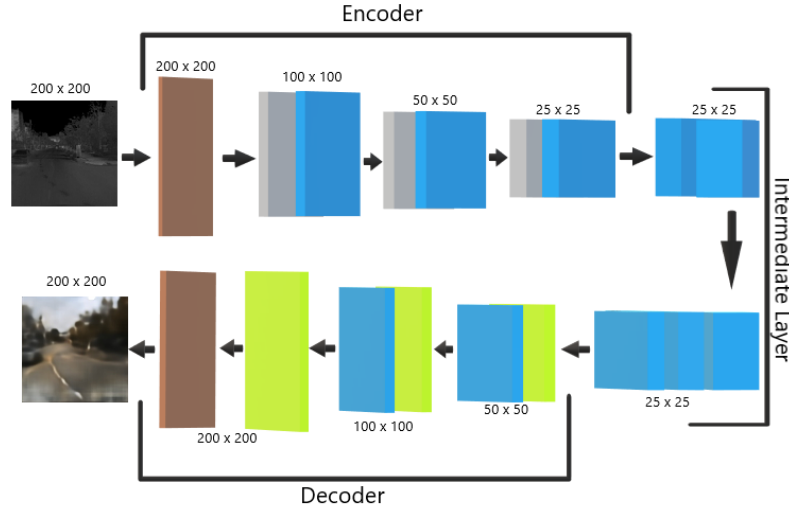


Figure 2: Architecture for the proposed encoder-decoder we have used in our work. The brown blocks refer to 2D convolution layers. Each of the blue blocks comprise of a 2D convolution layer which outputs a same sized patch, a Batch Normalization layer and a ReLU layer. The grey blocks contain a Convolution 2D which outputs a half sized patch, BatchNorm and a DropOut layer each. The blue blocks comprise of a Conv2DTranspose, BatchNorm and DropOut layers.

in [37] or directly using GAN for inter domain identification [40]. However, a point that needs to be understood on this matter is that GAN based models have their hyper parameters tuned to work on a specific domain (like faces), instead of generalized images, which is another factor we are focusing on in this work.

Additionally, since most of the previously mentioned works focus specifically on image colorization exclusively, none of them focus on the image registration method separately. While the paper by Yan et al. [10] does touch on this aspect, we found that when we took real world images, we could simplify the algorithm they provided. Without the different resolutions and scaling, it reduces to just a centre-shift problem, which is much less complex than the model we are proposing here. While this is similar to multi modal registration methods, most of such works like [35] focus on additional factors like corner detectors or use of localized voxels. The method we are proposing is much simpler in terms of computational complexity, while showing similar results.

We show in Fig. 3 and Table 5 that our results are better both qualitatively and quantitatively compared to [34], which is an improvement on the original encoder-decoder based technique [2]. Furthermore, as a part of the colorization technique, we show that it is possible to obtain good results even if we change the domain of images from Luminance-Chrominance (LA*B*) to RGB. This was inspired by our work on illumination enhancement for paintings [45], where we worked on the RGB domain and obtained very encouraging results. In order to show that the method we are proposing is in fact a good approximation to an optimal solution, we present extensive ablation studies in Table 5 where we compare scores for our

method with several changes in the proposed method. These are explained in Section 3.1.

In brief, our major contributions in this work comprise of:

- showing that there exists an optimal level of downscaling in an encoder-decoder past which results start degrading for a given database
- showing skip connections are not always better for encoder-decoder networks
- a new simplified method for registration of thermal images with their optical counterparts, which is robust enough to work even with images obtained from different thermal imagers with widely varying resolution of both optical and thermal images
- an optimal encoder-decoder architecture for creating a color mask so that new information can be produced for a thermal input in the form of color, which can then be fused with the thermal images to create a cross domain colorized image containing information from both the thermal and the optical images
- a new unique database [32] comprising of thermal-optical paired images from several different classes as well as their raw unscaled counterparts

2. Proposed Method

Our method is based on 3 separate modules which work serially to produce an output for a thermal image input. It can be formally broken down into 3 phases:

- Registration
- Colorization
- Post-processing

Of these, the first module (Registration) works only in the training phase whereas the next 2 modules work in both the training and testing phases. We are going to cover each of these sections separately in the following parts.

2.1. Registration

The registration module works on thermal-optical image pairs. The basic idea behind the registration module is that every image in the thermal domain has an optical counterpart. Since the thermal imagers we used have the option of capturing a thermal and an optical image of the same scene simultaneously, this is achievable.

However, the problems we encountered when dealing with a thermal-optical pair are that the thermal and the optical images were of different resolutions, and had a random centre shift based on the distance of the object being captured, since the physical location of the TIR and the optical sensors were different on the imager itself.

The FLIR imager had a 3.1 Megapixel optical sensor which produce images at a resolution of 1536x2048 pixels and the Sonel imager had a 5 Megapixel optical sensor which produces images at a resolution of 2592x1944 pixels. This means that for the same scene, the images captured by the FLIR imager were in landscape format while that by the Sonel imager were in portrait mode, and they were of widely different resolutions. So, we needed to formulate a method that would work uniformly across images from both imagers.

For this, we used the concept of Homography for the calculation of the scale of each image pair in the different thermal imagers. Homography tells us that in order to calculate the corresponding region that maps each x_i (data in the first domain) to its corresponding X_i (data in the second domain), we need to simply compute the 3×3 homography matrix [11]. Since we are dealing with 2D images, we consider the case where one image can be considered as the perspective projection of the other image. This is the standard method used for maps and aerial photography techniques. Once we had the factor, we could apply it uniformly across all images captured via that thermal imager. However, while the rescaling factors were the same for all images captured via a particular thermal imager, the factors themselves varied. The rescaling factor was 18% in case of the images captured via the Sonel thermal imager and 36.5% in case of the images captured via the FLIR thermal imager uniformly across both axes.

For obtaining the 4 corresponding points in 2 images from 2 different domains, we use LED lighting strips in order to create basic cases where we could obtain 4 different corresponding points of interest across the 2 differing domains easily, shown in Fig. 1. In that figure, (a) is the image obtained via the Sonel thermal imager, and (b) is the one obtained

via the FLIR thermal imager. Both optical images have an inset of the original thermal image at the bottom left to give an idea of the difference in scales between the captured thermal and optical images.

Once the rescaling problem was tackled and we obtained the factors for the images from the 2 different thermal imagers, we focused on the actual problem of registration. Now, while there are a lot of matching factors that are used as registration scores against similar images, we found that most of them were ineffective for our use. This is because registration techniques like Structural Similarity Index Measure (SSIM) work by matching how similar 2 images might be, which would not work in thermal-optical pairs since features present in optical domain (like painted patterns) might not be present in the thermal domain. The problems with matching techniques based on illumination, like Histogram Matching, however, are different. In these cases, the thermal and the optical pairs would behave differently because of the nature of the sensors. While optical domain images work on the principle of reflected light, the thermal sensors work on capturing the emitted radiation instead. This results in completely different illumination profiles for the same scene, which render illumination matching techniques useless.

However, we reasoned that the internal entropy of an image should be same regardless of the sensor used to capture the image since it represents the amount of disorder in an image. More intuitively, it represents the amount of information content in an image. Thus, we opted to use Mutual information (MI) as a matching score for the registration metric in our method. There has been a previous work on using MI for thermal-grayscale registration [13]. However, they showed that you would need to correct the illumination in both images for it to work. Our assumption, however, was that this would not yield any extra advantage to the thermal image as MI does not work with the absolute values of the illumination, but rather, with the distribution of the illumination. Of course, this is based on the fact that

the images are captured during the daytime, when the distribution can be clearly observed in both domains simultaneously, and would not work during night time.

We outline the algorithm (*Algorithm 1*) proposed for our Registration method as below. In it, N stands for the total size of the flattened rescaled optical grayscale image and K stands for the size of the thermal image. This is $384 \times 288 = 110,592$ for images captured via the Sonel imager and $240 \times 320 = 76,800$ for images captured via the FLIR imager. Once the region is calculated, the corresponding 2D index has to be calculated for the point on the resized optical image for obtaining the registered image, followed by reshaping it to the original 2D shape from 1D array.

In the below algorithm, $temp$ represents the score

that is used in order to decide the patch which needs to be registered in each iteration and MI represents the Mutual Information function which calculates the mutual information, given 2 distributions.

Algorithm 1

Input: Thermal-Optical image pair
Output: Cropped region of registered Optical image

1. *for each image pair in database:*
2. *flatten the thermal image as thermal*
3. *flatten the grayscale image as grayscale*
4. $temp = 0$
5. *for i in 0 to N-K:*
6. *if (temp < MI (thermal, grayscale[i to i+K]):*
7. *temp = MI (thermal, grayscale[i to i+K])*
6. *save image corresponding to x in 2D format*

In mathematical terms, the registration process becomes an optimization problem based on Shannon's entropy, which can be expressed as below. Given a matrix of the thermal image A with shape (a, b) and an optical image matrix X with starting index (x_i, y_i) , we can define a patch p_i where

$$p_i = (x_i : x_i + a, y_i : y_i + b) \quad (1)$$

as the (a, b) patch with the highest Mutual Information MI in the optical image and (x, y) being the shape of the image, where

$$\begin{aligned} 0 \leq a_i \leq x - a, \\ 0 \leq b_i \leq y - b \end{aligned} \quad (2)$$

since the values of a and b has to be bound between 0 and the last indices subtracted from the size of the image being considered for registration. We calculate the region with the highest Mutual Information in the optical image X based on the Mutual Information (MI) formula following *Algorithm 1*, where MI is defined as:

$$\begin{aligned} MI &= H(A) + H(X) - H(A, X) \\ &= \sum_{a \in A} \sum_{x \in X} p_{AX}(a, x) \log \frac{p_{AX}(a, x)}{p_A(a)p_X(x)} \end{aligned} \quad (3)$$

where $H(X)$ represents the entropy of system X . However, the calculation of MI is a very computationally expensive work. As such, we simplified the method by reducing the number of checks that need to be performed as a part of the search problem. Instead of searching the full optical image for the most optimal region corresponding to the thermal image, we change the range for the check to half of the difference between the 2 images. Thus, the range reduces from $(0 : x - a, 0 : y - b)$ to $((x-a)/2 - (x-a)/4 : (x-a)/2 + (x-a)/4, (y-b)/2 - (y-b)/4 : (y-b)/2 + (y-b)/4)$. We make an assumption here that the maximum amount of shift in pixel would not be more than half the total difference in sizes between the 2 images. This is also shown to be valid experimentally for both imagers when we take

an image at a very close range and check the parallax error present between the thermal and the resized optical images. We show this as Fig. 1 in the Supplementary materials section. However, while we can reduce the time complexity by about 50%, we found that there were a lot of redundant checks being performed as a part of the checking procedure because after the maximal region is found, the whole loop continues till the end of the range.

Thus, we introduced a secondary check to this wherein the checking process only continues until 3 full rows of the checking range is skipped without any update to the maximal region. We base this on the assumption that the check for the maximal MI region happens gradually, wherein the optimal region is found out by closing the gap in maximal region. Thus, if there is a break in the check region, it means that the maximal region has already been achieved, and further comparisons need not be performed. This brings in a very major change in the time complexity, reducing the average time by a factor of 91%. We name this *Algorithm 2*. We include the full algorithm in the Supplementary Section.

However, we deduced that this could be reduced further, so we made a few more modifications to the process, reducing the time complexity even further. Now we take a region that is 30 pixels away from the edges of the thermal image in each direction. This is because we can see that the thermal band is present in all thermal images towards the right most region. Not only that, we try to capture the images with maximal information regions at the centre of the thermal image. Thus, by trimming the sides of the thermal image theoretically does not result in a significant loss of information contained in the region to be compared. Finally, we cut out the registered optical image from the rescaled RGB matrix as:

$$Image_i = (x_i - 30 : (x_i - 30) + a, y_i - 30 : (y_i - 30) + b) \quad (4)$$

This process brings down the registration time complexity further by a factor of 32% from the previous iteration. We call this *Algorithm 3*, and is the final registration algorithm we are proposing in this work. We include a bar graph showing the time complexity comparison of *Algorithm 1-3* in Fig. 2 in the Supplementary section.

It needs to be understood however, that our method does not work for all pairs of thermal-optical images. This is covered in more detail in Section 3.4.

2.2. Colorization

While most of the deep learning based colorization techniques focus on using the Luminance-Chrominance image model to work on images, our idea was different. Although earlier papers [14], [15], [9], [2] show that the LAB model is easier to work with for colorization techniques, they were all based on the idea that only the

chrominance values need to be calculated while the luminance values can be directly transferred from the grayscale image. While this method would work for the colorization of optical domain grayscale values, it becomes clear that the method would fail in case of colorization of thermal images where the optical grayscale images and the thermal grayscale images differ significantly from each other. Thus, instead of the LAB domain, we chose to work directly in the RGB domain instead. This not only creates an output with equal focus on the chrominance and the luminance channels, the output luminance channel is merged with the thermal inputs to create the final fused image. This is covered in more depth in Section 2.3.

Our method for colorization is a deep learning network. The basic framework for the network is based on the work described in [2] which works on the principle of a simple encoder-decoder for the calculation of the luminance- chrominance values from a grayscale prior. We modify it significantly to produce a mask directly in the RGB domain, which is then fed into the post processing step for creating the final colored image. Several changes like using a Conv2DTranspose layer instead of upsampling layer (so that the gradient information is better preserved during back propagation of loss) and checking the effectiveness (and thus eliminating) the skip connections have been implemented. More details on this can be found in Table 1-4. We also make a post processing step which ensures that the final output contains the data from both the thermal and the optical domain concurrently in the same output image. This is detailed in Section 2.3.

We divide the network into 3 subsections, namely Encoder Layer, Intermediate Layer and Decoder Layer in order to better describe it (Tables 1 –4).

Table 1: Building blocks (Input: nxn)

Layer Name	Details	Output
half block	Conv2D {W (3,3), S: (2,2)} BatchNorm Relu	$\frac{n}{2} \times \frac{n}{2}$
double block	Conv2DTranspose {W: (3,3), S: (2,2)} BatchNorm DropOut	$2n \times 2n$
same convblock	Conv2D {W (3,3), S: (1,1)} BatchNorm Relu	$n \times n$
same deconvblock	Conv2D {W (3,3), S: (1,1)} BatchNorm DropOut	$n \times n$

Table 2: Encoder Layer (Input: 200x200x1)

Layer Name	Details	Output
Block1 (D:1)	Conv2D {W (3,3), S: (1,1)}	200x200
Block2 (D: 128)	half block	100x100

Block3 (D: 128)	same convblock	100x100
Block4 (D: 256)	half block	50x50
Block5 (D: 256)	same convblock	50x50
Block6 (D: 512)	half block	25x25
Block7 (D: 512)	same convblock	25x25

Table 3: Intermediate Layer (Input: 25x25x512)

Layer Name	Details	Output
Block8 (D:1024)	same convblock	25x25
Block9 (D:2048)	same convblock	25x25
Block10 (D:2048)	same convblock	25x25
Block11 (D:1024)	same convblock	25x25
Block12 (D:512)	same convblock	25x25

Table 4: Decoder Layer (Input: 25x25x512)

Layer Name	Details	Output
Block13 (D:256)	double block	50x50
Block14 (D:256)	same convblock	50x50
Block15 (D:128)	double block	100x100
Block16 (D:128)	same convblock	100x100
Block17 (D:64)	double block	200x200
Block18 (D:3)	Conv2D {W: (3,3), S: (1,1)}	200x200

In the Tables 2-4, D represents the depth (or the number of layers) of the network at the corresponding level, W stands for the shape of the sliding window and S is the stride. N stands for the number of outputs in the case of the Dense layers and represents the number of times the previous layer is repeated in case of a Concatenation layer. Conv2D represents a 2D Convolution layer, BatchNorm is the Batch Normalization layer, LReLU is a Leaky ReLU layer and DropOut is a Drop-out layer. All DropOut layers have a parameter of 0.5.

The deep learning network that we use (Fig. 2) for the translation of the thermal image into an RGB mask is an end to end colorization technique which produces a unique output for a given grayscale thermal input. We use *elu* as an activation function in the first convolution layer and in all of the Conv2DTranspose layers. The encoder Conv2D layers do not have any activation as we add ReLU layers after them. The last layer activation is sigmoid since the output is on a range of [0,1] as we normalize the RGB values for all the 3 channels of

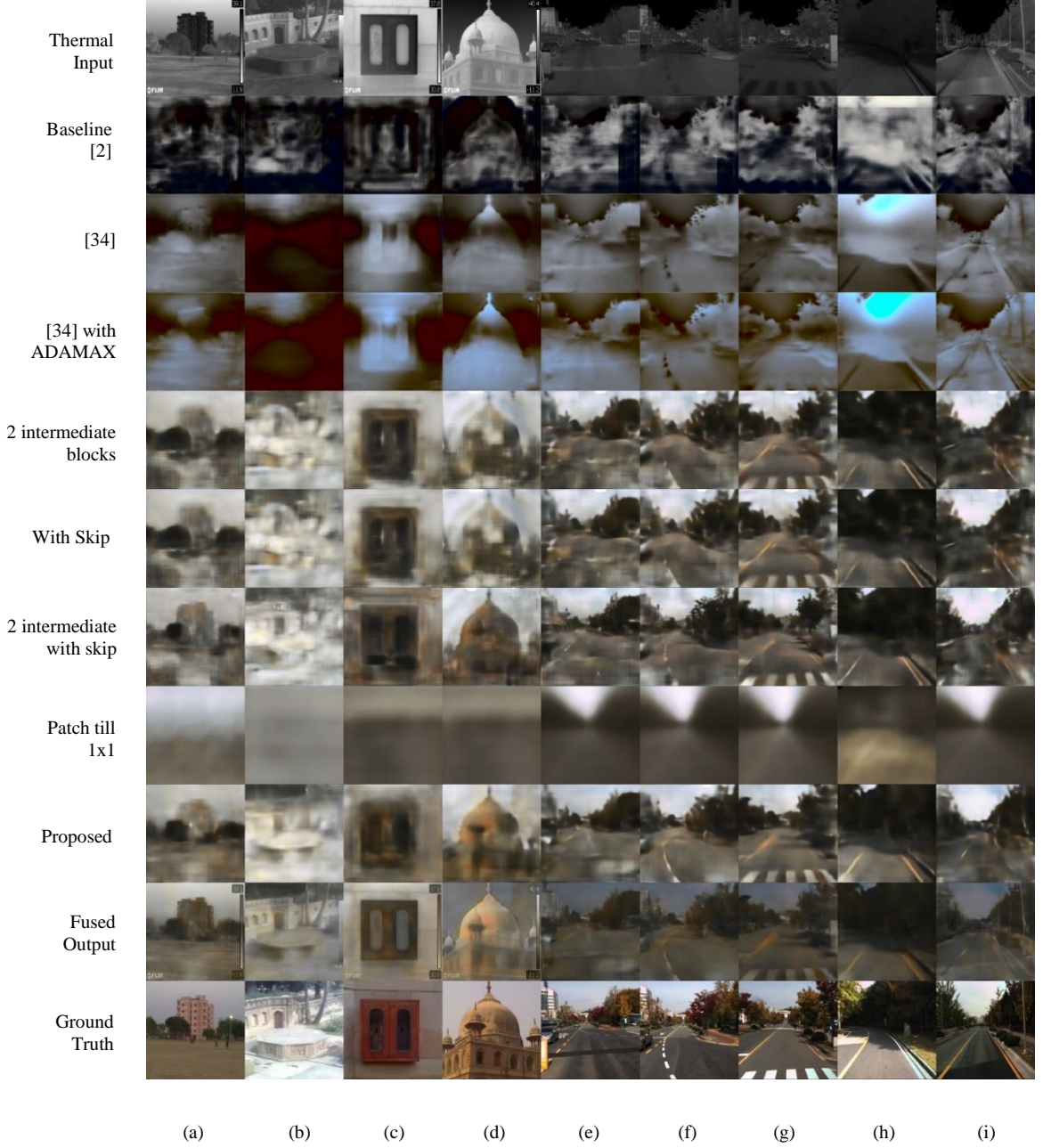


Figure 3: Comparative Analysis of Results. The first row represents the raw thermal images, second till 8th row provides the outputs obtained from the deep networks for the different models. The ninth row represents the RGB output mask obtained via the proposed network while the 10th row represents the output obtained after fusion. The last row shows the ground truth obtained via the optical sensor. Full sized image is presented as Fig. 3-4 in the Supplementary Section.

the output images by dividing the individual values at the 3 different layers by 255, to normalize them.

After the intermediate layer, we finally start upscaling the layers via 2D transposed convolution in the decoder layer while, at the same time decreasing the depth of the output so that we obtain the final RGB mask, which needs to be fused back with the infrared thermal input image to obtain the colorized fused image as the output.

The input to the network is a 200x200 image, irrespective of what the initial thermal image size may be, so that we have a parity of inputs in the model. Since it is a grayscale image, it has only 1 layer while the output is a 200x200x3 RGB image.

As can be seen from the architecture, we increase the depth of the layer in steps. Each of the blocks deal with a fixed depth of output while halving the dimensions till we reach a fixed size and simply increase the depth up to 2048, finally doubling the size at each level and decreasing the depth. For halving the shape of the input, we use convolution layers directly. It is to be noted here that unlike the original paper by Berg et al., we do not use the *upsample* layer for our work, rather opting for convolution transpose layer. The benefit of this is the fact that the transpose layer retains the weights, thus providing a link between the original input

across the layers and the output which is double the size of the input in the 2 axes.

We use *logcosh* as the loss function with ADAMAX as an optimizer for our network. Detailed explanation as to why we are using *logcosh* is discussed in Section 3. Once the network is trained, we can input a thermal grayscale image and obtain an RGB mask for the input image. The mask is combined with the thermal input image in the post processing layer to obtain the final colorized output.

For our ablation studies presented in Table 5, we use variations of this base deep network in order to obtain the RGB masks. These networks range from increasing the length of the encoder (and decoder layers) by halving the shape till it reaches a patch size of 1x1, introducing skip connections in the network and changing the number of intermediate layers, among others. A detailed discussion of these networks along with their results are presented in Section 3.

2.3 Post Processing

Once the mask is obtained for an input, we need to create the final output in the form of a colorized image from it. This is the post processing step. The postprocessing step can be further divided into 3 sub-steps. They are:

- Conversion to LAB domain
- Fusion of Thermal Image
- Conversion back to RGB domain

Our theory was that the mask, obtained in the RGB domain contains the chrominance information for an input thermal grayscale image. Thus, while creating the final colorized image, we gave an equal priority to the thermal image input for preparing the final output. For the first step, we take the RGB mask and convert it into LAB domain. This is because at this stage, we wish to incorporate the information from the thermal image as the luminance channel into the output in order to create the final cross domain colorized image. For this to be successful, it is important to separate the chrominance from the luminance value of the output mask. However, we did not want to discard the luminance information contained in the mask completely either. Thus, comes the second stage. Once we obtain the luminance information of the output mask, we fuse it with the thermal image according to the equation given below:

$$L = (l + thermal) / 2 \quad (6)$$

In Eq. 6, L represents the final luminance channel of the output image, l stands for the mask luminance channel and *thermal* represents the thermal image. This equation incorporates the thermal image information into the final colorized output. Once the luminance channel is ready, we just fuse it together with the chrominance channel and convert it back

from the LAB domain into the RGB domain. The range of all 3 variables are normalized to [0,255] to achieve this

While there have been works on fusion of thermal and visible images like in [41], those are focused on separate problems, like foreground detection in fused images, whereas our method focuses on imparting information to thermal images through data synthesis. Moreover, these fusion related works focus on grayscale images, which is very different from our objective as well.

3. Experimental Results and Discussion

The general structure presented in [2] is a basic encoder decoder with skip connections. This is used for colorization of thermal images and the authors present very good results obtained with this architecture. However, the database used for this experiment is the KAIST Multispectral pedestrian database [3] which is a collection of consecutive frames obtained from videos of pedestrians jointly in the thermal and the optical domain. What this results in is that the images are very similar to each other. This means that the mean difference between the data points become very low, which would not be sufficient for testing our hypothesis on whether different configurations of the encoder-decoder structure would affect the final output.

This is why we created a database containing registered 1843 thermal to color paired images. Next we had to consider the problem of the base image size which we would use in order to train the network. Since we were using an encoder-decoder structure, we had to keep the input and output images in same dimension. The problem however was that the FLIR thermal imager has a maximum resolution of 240x320 for the thermal images, which is why we opted to create 200x200 images across both imagers and used that resolution in our network. We add in the images from Set 00 to Set 04 from KAIST MS dataset to our training images. This resulted in an additional 50189 thermal-optical pair of images in addition to our 1843 images, for a total of 52032 images. Out of this, we use 100 images from our dataset, chosen randomly for testing and the rest for training. All 50189 images from KAIST MS dataset have been used for training as we used Set 06 from the KAIST MS dataset, containing a total of 12987 images for testing. This resulted in a separate pool of images for training and testing and ensured that there were no overlapping images between the 2, which could bias the output.

We wanted to compare our results against the TIR2Lab results presented in the paper [2], the code that the authors presented publicly did not work properly on our end. We attributed this to the fact that they had stated on their page that it was still in development stage and might not work properly. As such we sent a few data points directly to the authors so that they may test it on their end and mail us the

results. However, the authors said that they were unable to provide the output, citing other engagements on their part. Hence, we reproduce their code independently and provide the baseline results in their paper for the same database as outlined in [2]. In order to ensure that there were no biasness on our method, we use inbuilt TensorFlow metrics for calculating both the Mean Squared error and the DSSIM error, which have been used in both works. Additionally, we would like to state that for reproducing the work in [34], we had to restructure the output layers by cropping a layer at a few levels to ensure that the output shapes matched (since halving 200 continuously reaches 25 and then 13, and the double of 13 via upsampling provides 26 instead of 25). We used the same process in our own method, where we go down to 1x1 patch size for our ablation study presented in Table 5. Lastly, we take the values for α and β as 0.33 and 0.67 for the combined error that they describe in [34] since the values were not mentioned in their work. 0.33 refers to the weight used for the luminance layer and 0.67 refers to the weight used for the chrominance layer loss calculation. This is based on the rationale of distributing the weights according to the number of layers in luminance and chrominance (1 and 2 respectively) proportionately.

We choose \logcosh as the loss function in our deep learning method because the operational values become very small after normalization and lie between (0,1). This simplifies the calculation by directly changing the values under consideration by making $\log(\cosh(x))$ approximately equal to the value shown in Eq. 7:

$$\logcosh(x) = \begin{cases} \frac{x^2}{2}, & \text{for } x \ll 1 \\ |x| - \log(2), & \text{otherwise} \end{cases} \quad (7)$$

In our case, since we are dealing with the sigmoid layer at the last layer, all of our output values are confined to the range of [0,1]. Thus, we can safely assume that since our output values are small enough, the \logcosh loss will always approximate to the $\frac{x^2}{2}$ value. Moreover, in order to keep parity and make the loss converge faster, we opt for an activation function of elu or provide a $ReLU$ layer at results in Table 5. We also show our result against the method detailed in [34], which reports better every block.

This is because the elu activation function is defined as:

$$ELU(x) = \begin{cases} x, & x > 0 \\ \alpha(e^x - 1), & x < 0 \end{cases} \quad (8)$$

This, combined with the \logcosh loss ensures that the values of the network always stay in the exponential plane. This is relevant because in the standardized RGB system, which is used by display systems, the value of luminance is based on Gamma correction, represented by Eq. 9:

$$V_{out} = A V_{in}^\gamma \quad (9)$$

where γ represents the variable value in question for the output luminance value for individual R, G and B channels. In general cases, the value of A is taken as 1 and the inputs and outputs are typically in the range of 0-1, as is the case with our deep network.

In the standardized sRGB system, the value of gamma cannot be expressed as a single numerical value and it is usually expressed as an average value of around 2.2 with a linear ($\gamma = 1$) near black and it varies elsewhere as a log input to an output space with an exponent of 2.4. Thus, combining Eq. (7), (8) and (9), we can generalize our loss function as:

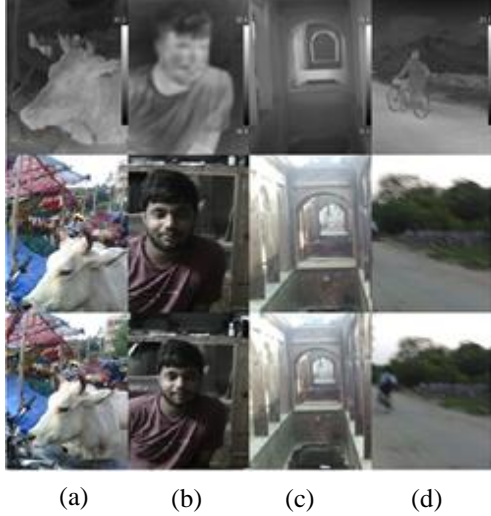
$$\text{loss} = \alpha x^n \quad (10)$$

which can be expressed as AV^γ . This is equivalent to the gamma value needed to represent the R, G and B values in the sRGB model. Hence, as we are aiming to use the RGB values directly in our network, we opt for \logcosh as our loss function.

Lastly, for the optimizer, we use ADAMAX instead of ADAM as in [2] and [34] because we are using a database which instead of using images which are all similar in nature, uses sparse values (around 4.5% of the total images) which are completely different in nature. Thus, instead of using a vector value which is a combination of the past and current gradients, it calculates the maximum of the two by using the L_∞ norm [43]. What this essentially means is that when significant gradient updates are required, they can be done, but only when these values are actually required, when compared to the past gradients.

Our hypothesis, while designing this experiment was that when we are dealing with images where we need to create an output in a completely different domain (from grayscale NIR to optical RGB in this case), the respective mapping needs to be relevant. Thus, if we start considering ever smaller patches of an image, we would overshoot the point at which a patch of the input image would stop being relevant. That is, our assumption was that there is a minimum size of patch needed which would make an image recognizable. This is supported by the work [42] as well. However, the general structure of encoder-decoder used usually halves the patch size till it reached 1x1 and then upscales it from there. While this would be relevant when the data used for the

experiment is similar to each other (as in the case of KAIST MS dataset), this would stop being useful as soon as we introduce some data points which deviates completely from the standard pattern, thus leading to generalization. In fact, this can be seen in [2] and [34] which are basically the same work, wherein [34] reports a better result by simply going down to a patch size of 1x1. However, as can be noted from Table 5, we can see that the results from our experiments yield results which clearly show that this is not effective. This is discussed in more



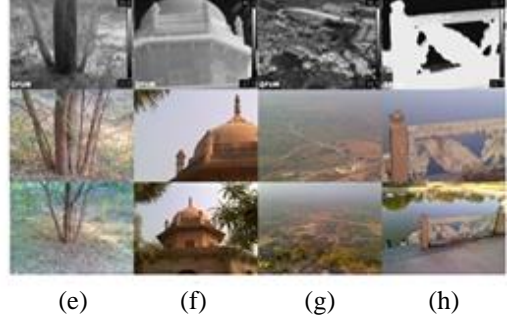
(a) (b) (c) (d)

details in Section 3.1 as well. However, we do not stop with just this. Our second hypothesis was, in case of regression deep networks, used for data modelling (like creation of RGB data from grayscale input), skip connections might not necessarily be a good thing at every step since the data distribution of the input differs widely from the data distribution of the output (on account of being from 2 different kind of sensors: NIR and optical in this case). Again, this comes down to the data used in order to model a network, but when we are considering generalization of data as a major point in the design of a deep network, this cannot be ignored. In fact, this is also shown by the results we present in Table 5, which is discussed in further details in Section 3.1.

We would like to state here that while we found one other instance of a large dataset of thermal images from the Military Sensing Information Analysis Center (SENSIAC) [31] used in [33], it often obtained via very high-grade state of the art cameras, which are not feasible for general use. Finally, the dataset is not publicly available, and needs a fee for its usage.

3.1. Quantitative Analysis

The quantitative analysis of the results are shown in Table 5. We are presenting the comparison of the scores obtained from the images from our method along with the baseline scores obtained from [2] and the scores obtained from [34], which is reported as having obtained better results in comparison to [2]. We also include scores from [34], trained with ADAMAX instead of ADAM, showing that the scores are almost similar, but yield different image outputs, shown in Fig. 3. Along with the above methods, we include the proposed method, and several variants of the proposed method as different points of comparison. The first of these methods checks if the number of intermediate layers would make a difference. Instead of having 5 intermediate layers, would having 2 make a difference is the question this tries to answer. The next one checks if



(e) (f) (g) (h)

Figure 4: Images where the Registration algorithm is unable to provide a perfect match of thermal-optical pairs in case of images captured via the Sonel thermal imager for (a) – (d) and those captured by the FLIR thermal imager for (e) - (h)

adding skip connections in the proposed method, with skip connections added between the encoder and the correspondingly sized decoder blocks would be helpful. The next one checks if the combination of the previous 2 would have a better result and the last one is meant to check the effect of downsampling the patch size to 1x1, but without the use of any skip connections.

We have chosen 4 different scores of comparison for our methods. These are the L1 score, or Mean Absolute Error (MAE), the Root Mean Square Error (RMSE), Peak Signal to Noise Ratio (PSNR) and the Structural Similarity Index Measure (SSIM). The first 2 are simple scores which show how far the images are in the data space from their optical counterparts, the PSNR is meant to compare the noise introduced as a result of the respective measures and the SSIM checks how similar each layer of the RGB images are to the optical outputs they are trying to create. We include the lowest value, the average value and the highest value for each method. As can be observed, except for the L1 score, every other metric has the best average value for our proposed method. The nearest values to our proposed method scores are observed in the network created with skip connection in addition to our proposed network. However, even if the scores denote a close value, if we observe the images created in Fig. 3, we can clearly observe that our method provides better results. We discuss this further in Section 3.2.

We denote the best values (the lowest scores for L1 and RMSE difference scores and highest values for SSIM an PSNR scores) in blue and the worst scores in red in Table 5. The best average scores are denoted in bold. Even though the low and high scores for correspondingly L1 and RMSE and PSNR and SSIM values are better for the results obtained from [34] in comparison with [2], we can see that the average value for L1, RMSE and PSNR is better for the work presented by Berg et al. in comparison to [34]. This indicates that the outputs obtained from [2] are more stable in comparison to those obtained

by [34]. This is in also in line with our conjecture that going down to the lowest 1x1 patch might not be the best option.

This score table proves our point that there is an optimal level of patch size for an encoder-decoder method, given a particular database below which the output starts degrading instead of improving. This is in line with the hypothesis that there is a size of patch below which information cannot be further quantized for a given image. This is the reason why the work presented in both [2] and [34] provided very good results when trained with just the KAIST MS dataset, but failed to provide results that were as good as we have been able to obtain. The average values for L1, RMSE and the PSNR score between [2] and [34] also supports this argument since the improvement that [34] reports on [2] is going down to a patch size of 1x1 (with the corresponding skip connections added in).

As can be observed, the scores for the proposed method extended to 1x1 exhibit some of the worst values in the table, although for RMSE, it also exhibits the best singular value, denoting that the scores fluctuate a lot, and thus, an unstable, and thus, not very well constructed deep network. The proposed method, incorporated with skip connections provides values which are almost similar to the values obtained from the proposed network, but other than the image analysis presented in Section 3.2, the question arises as to why would one want to incorporate more complexity in a network when the values are so close to each other by incorporating concatenating layers. Further, when we compare the values between the proposed method with skip connections, the one with just 2 blocks in intermediate layer and a combination of the 2, in none of the cases does the combination network work better than either of the 2, showing that simply increasing complexity in an encoder-decoder structure does not guarantee a better output.

3.1. Qualitative Analysis and Discussion

In Fig. 3, the first row denotes the thermal images rescaled to 200x200, which are used as inputs to the deep network shown in Fig. 2. These are grayscale images which go from cold black (pixel value of 0) to white hot (pixel value of 255). This means that the thermal images are always histogram equalized by default since it occupies the whole [0-255] range of pixel values for every image.

The second row shows the outputs from the baseline method of [2]. As can be seen in these images, while the general shape of the output is being created, the images themselves tend to be more of grayscale rather than containing color information. For example, for image (d), we can see that the structure of the building is clearly coming through, as is the case for the last image as well. However, as we can note from Table 5, this scores best for the L1 difference values, indicating that the output images

themselves, while not being very perceptually clear, lie close to the output optical images on the data plane.

For rows 3 and 4, we show the outputs obtained from the method presented in [34] and a variation of the same, where we change the optimizer from ADAM to ADAMAX. As we can see, the color information changes visibly between the 2 rows, and is most visibly noticeable in column (d) and (g), wherein the images for ADAMAX seem to be more prominent.

Row 5 onwards, we have the outputs from the different variations of our networks present. The 5th row shows outputs when we use only 2 intermediate blocks instead of 5. The next row shows what the output will be like if we used our network with skip connections between the encoder and the decoder blocks while the 7th row shows a combination of these 2. The next row provides outputs on what the output will be like if we used patch till 1x1 levels for the encoder and then convolution transposed is back to the input size. The 9th row shows our proposed network outputs, the 10th shows the fused images we are creating and the last row shows the optical images against which we train our network.

It is immediately apparent from these images that among our networks, the 1x1 network exhibits the worst output images. However, this is despite the fact that in Table 5. For RMSE values, it provides the best singular value (and the worst one as well). The 5th and the 6th rows exhibit similar outputs, and it gets perceptibly better for the 7th row, despite the fact that the 6th row scores exhibit the second best values. However, looking at image (a), (d) and (f), we can immediately see that they are better.

The proposed method provides better image outputs visually. This is because if we look at image (d), we can see that the color of the sky and the color of the building closely match the optical output as compared to the 7th row images. It is the same for image (f) and (g), where the lines on the roads have a better clarity. Image (i) also provides much better color information in this case as is evident from the clarity of the road section.

In the 9th row, we show the fused outputs, where the images contain information jointly from the thermal and the optical images. These are created by combining the thermal input images the output masks in row 9 according to Eq. 6. This jointly provides the clarity provided by the thermal inputs while retaining the information provided by the optical RGB masks, creating a new type of image. The full sized image of Fig. 3 is presented as Fig. 3-4 in the Supplementary Section for better clarity.

3.1. Limitations

While our method seems to work with most data, it fails in few cases. The first is the failure at the registration module. We see that in the case of data where the subject is moving, the thermal and the

Method	Measure	L1	RMSE	PSNR	SSIM
Baseline [2]	Average	142.86	17.76	27.91	0.14
	Low	91.25	16.96	27.68	0.03
	High	179.83	18.23	28.31	0.27
Method presented in [34]	Average	149.70	17.94	27.83	0.24
	Low	85.27	16.09	27.49	0.05
	High	193.49	18.64	28.78	0.42
Method presented in [34] with ADAMA X	Average	149.60	17.96	27.82	0.23
	Low	85.29	15.89	27.49	0.03
	High	195.17	18.64	28.89	0.42
Proposed Method with 2 blocks in Intermediate Layer	Average	146.52	17.02	28.29	0.45
	Low	65.17	15.25	27.60	0.14
	High	211.47	18.39	29.24	0.67
Proposed Method with Skip Connections	Average	148.14	16.96	28.32	0.48
	Low	54.30	14.50	27.61	0.15
	High	216.66	18.38	29.70	0.75
Proposed Method with 2 blocks in Intermediate layer and Skip Connections	Average	147.18	16.98	28.31	0.46
	Low	58.18	14.72	27.60	0.15
	High	210.25	18.40	29.57	0.71
Proposed Method with downsampling to 1x1	Average	154.10	17.18	28.22	0.45
	Low	63.73	14.35	27.45	0.16
	High	212.25	18.72	29.76	0.72
Proposed Method	Average	148.24	16.91	28.35	0.49
	Low	63.73	14.55	27.59	0.15
	High	215.69	18.43	29.66	0.70

Table 5: Quantitative Analysis of the results obtained by the different methods

optical sensors are unable to capture the same image. This can be seen in Fig. 4 (b) and (d).

This occurs because there is a lag in the operation time of the thermal and the optical sensors as the 2 work serially. Subsequently, the data captured is different in the 2 cases. While we see that this does not affect the registration directly in some cases (where the subject of movement is very small in comparison to the background), we do not take these cases in consideration while preparing the training set. This is because our work deals with colorization and if the difference in images attributed due to the motion between the images of the input and the output domain become too large, the deep network cannot learn the necessary parameters needed to create the color mask from the input.

The second case where the registration module fails to provide an accurate registration for an input is in case of a parallax error, as can be observed in Fig. 4 (c). The optical and the thermal sensors are physically located at different locations in both the thermal imagers we have used for creating our database. This creates a shift in the image being captured. We observed that while this does not create much of an error when the objects being captured are far away, at nearby distances, it becomes a major issue. In fact, the image captured becomes completely different when the object is very close to the imager, creating a shift in perspective, thus making the algorithm we have provided being unable to provide a good match. We can notice that in Fig. 4 (c), the arches change in their perspective between the thermal and the optical images altogether and in Fig. 4 (f), we can see that the leaves on the right side of the structure change the image between the thermal and the captured optical images.

Another problem that we have faced is that some images are highly bleached. By ‘bleached’, we mean that there is not sufficient difference in the different surfaces of the object in the thermal image. This is primarily the case when we deal with objects which are left for too long at a certain temperature (for example, an animal sitting in the sun). This can be seen in Fig. 4 (h) and (a). In the first one, you can see that due to the extreme difference between the foreground and the background, there is a distinctive loss in features in the image, while in the second case, the background becomes blurry, creating a case where the Mutual Information based algorithm is unable to get enough unique information to create a good match.

Finally, the last case where we see problems with registration is where there is a loss of data due to the sensor being unable to capture precise data. This can be seen in Fig. 4 (e) and (h). In case of Fig. 4 (e), we can see that the small branches in front of the tree are not captured in the thermal image, thus creating a different image for the algorithm, while in (h), the optical sensor is unable to capture the correct image

corresponding to a thermal map due to fog and imperfect illumination. A case the deep network might fail is with too much illumination, bleaching out details in the photograph.

All of our data is available for public use in IEEE Dataport at [32]. We have also included the raw data for the unregistered images in the database so that others may yet use them in further researches in other avenues.

4. Conclusion

We have presented a method which has been trained with data from Prayagraj (Allahabad) city in India for the modern setting based images and jointly from Chitrakoot and Prayagraj for the historical buildings images and the greenery data. The crowd data is collected from the Maha Kumbh Mela 2019 that occurs once every 12 years at Prayagraj. It is the biggest fair on earth and to our knowledge, this is the only dataset that contains images from it. The data was collected over a period of 1.5 years and collated together.

We have been able to use only 1843 images as a part of the diverse dataset we have presented in [32] as of now, and it is expected that the results would improve once more data is added to this database. Another course of study that can be performed is the effect of movement in thermal images and how it affects the results. However, since that needs a separate specific database, we have not attempted it as part of this paper and aim to include it as part of a future work.

All experiments were carried out on a machine with i5 7600 processor with 16 GB RAM and a RTX 2080 Super with 8 Gbps GDDR6 memory. All coding was done on Python with Keras 2.2.4, using Tensorflow 1.13.1 as the backend. On an average, one epoch of proposed took about 21 minutes to complete. The proposed algorithm reached loss saturation by the 29th epoch. The thermal imagers used were FLIR E40 and Sonel KT400.

5. Acknowledgements

We would like to thank the DIPR Lab, DRDO, Government of India for funding this research under grant number 2535/DIPR-II/MD/CARS-01 and Computer Visions and Biometric Lab (CVBL), IIIT Allahabad for providing the necessary facilities to conduct it. We would also like to thank Prof. Gaurav Sharma, University of Rochester, New York, USA for his expert guidance on the research work and Mr. Nand Kumar Yadav, IIIT Allahabad, without whose help the data collection drive would never have been completed.

References

[1] Tang, Jun. "A color image segmentation algorithm based on region growing." In 2010 2nd International Conference on

Computer Engineering and Technology, vol. 6, pp. V6-634. IEEE, 2010.]

[2] Berg, Amanda, Jorgen Ahlberg, and Michael Felsberg. "Generating visible spectrum images from thermal infrared." In Proceedings of the IEEE Conference on Computer Vision and Pattern Recognition Workshops, pp. 1143-1152. 2018.

[3] S. Hwang, J. Park, N. Kim, Y. Choi, and I. S. Kweon. Multispectral Pedestrian Detection: Benchmark Dataset and Baseline. In 2015 IEEE Conference on Computer Vision and Pattern Recognition (CVPR), pages 1037-1045. IEEE, jun 2015.

[4] Kuang, Xiaodong, Xiubao Sui, Chengwei Liu, Yuan Liu, Qian Chen, and Guohua Gu. "Thermal Infrared Colorization via Conditional Generative Adversarial Network." arXiv preprint arXiv:1810.05399 (2018).

[5] Arjovsky, Martin, Soumith Chintala, and Léon Bottou. "Wasserstein gan." arXiv preprint arXiv:1701.07875 (2017).

[6] Salimans, Tim, Ian Goodfellow, Wojciech Zaremba, Vicki Cheung, Alec Radford, and Xi Chen. "Improved techniques for training gans." In Advances in neural information processing systems, pp. 2234-2242. 2016.

[7] Metz, L., B. Poole, D. Pfau, and J. Sohl-Dickstein. "Unrolled generative adversarial networks (2016)." arXiv preprint arXiv:1611.02163.

[8] Poole, Ben, Alexander A. Alemi, Jascha Sohl-Dickstein, and Anelia Angelova. "Improved generator objectives for gans." arXiv preprint arXiv:1612.02780 (2016).

[9] Iizuka, Satoshi, Edgar Simo-Serra, and Hiroshi Ishikawa. "Let there be color!: joint end-to-end learning of global and local image priors for automatic image colorization with simultaneous classification." ACM Transactions on Graphics (TOG) 35, no. 4 (2016): 110.

[10] Yan, Bin, Xiangshan Kong, Fuyou Jiang, Peng Xu, and Hui Yuan. "Multi-Spectral Stereo Image Matching Based On Adaptive Window." In 2018 International Conference on Advanced Control, Automation and Artificial Intelligence (ACAAI 2018). Atlantis Press, 2018.

[11] Dubrofsky, Elan. "Homography estimation." Diplomová práce. Vancouver: Univerzita Britské Kolumbie (2009).

[12] Liu, Lixiong, Bao Liu, Hua Huang, and Alan Conrad Bovik. "No-reference image quality assessment based on spatial and spectral entropies." Signal Processing: Image Communication 29, no. 8 (2014): 856-863.

[13] Li, Jing, Quan Pan, Tao Yang, and Yong mei Cheng. "Color based grayscale-fused image enhancement algorithm for video surveillance." In Third International Conference on Image and Graphics (ICIG'04), pp. 47-50. IEEE, 2004.

[14] Suárez, Patricia L., Angel D. Sappa, and Boris X. Vintimilla. "Learning to colorize infrared images." In International Conference on Practical Applications of Agents and Multi-Agent Systems, pp. 164-172. Springer, Cham, 2017.

[15] Cheng, Zezhou, Qingxiong Yang, and Bin Sheng. "Deep colorization." In Proceedings of the IEEE International Conference on Computer Vision, pp. 415-423. 2015.

[16] Levin, Anat, Dani Lischinski, and Yair Weiss. "Colorization using optimization." In ACM transactions on graphics (tog), vol. 23, no. 3, pp. 689-694. ACM, 2004.

[17] Luan, Qing, Fang Wen, Daniel Cohen-Or, Lin Liang, Ying-Qing Xu, and Heung-Yeung Shum. "Natural image colorization." In Proceedings of the 18th Eurographics conference on Rendering Techniques, pp. 309-320. Eurographics Association, 2007.

[18] Welsh, Tomihiisa, Michael Ashikhmin, and Klaus Mueller. "Transferring color to greyscale images." In ACM transactions on graphics (TOG), vol. 21, no. 3, pp. 277-280. ACM, 2002.

[19] Gupta, Raj Kumar, Alex Yong-Sang Chia, Deepu Rajan, Ee Sin Ng, and Huang Zhiyong. "Image colorization using similar images." In Proceedings of the 20th ACM international conference on Multimedia, pp. 369-378. ACM, 2012.

[20] Larsson, Gustav, Michael Maire, and Gregory Shakhnarovich. "Learning representations for automatic colorization." In European Conference on Computer Vision, pp. 577-593. Springer, Cham, 2016.

[21] Huang, Yi-Chin, Yi-Shin Tung, Jun-Cheng Chen, Sung-Wen Wang, and Ja-Ling Wu. "An adaptive edge detection based colorization algorithm and its applications." In Proceedings of the 13th annual ACM international conference on Multimedia, pp. 351-354. ACM, 2005.

[22] Cao, Yun, Zhiming Zhou, Weinan Zhang, and Yong Yu. "Unsupervised diverse colorization via generative adversarial networks." In Joint European Conference on Machine Learning and Knowledge Discovery in Databases, pp. 151-166. Springer, Cham, 2017.

[23] Deshpande, Aditya, Jiajun Lu, Mao-Chuang Yeh, Min Jin Chong, and David Forsyth. "Learning diverse image colorization." In Proceedings of the IEEE Conference on Computer Vision and Pattern Recognition, pp. 6837-6845. 2017.

[24] Guadarrama, Sergio, Ryan Dahl, David Bieber, Mohammad Norouzi, Jonathon Shlens, and Kevin Murphy. "Pixcolor: Pixel recursive colorization." arXiv preprint arXiv:1705.07208 (2017).

[25] Royer, Amelie, Alexander Kolesnikov, and Christoph H. Lampert. "Probabilistic image colorization." arXiv preprint arXiv:1705.04258 (2017).

[26] Limmer, Matthias, and Hendrik PA Lensch. "Infrared colorization using deep convolutional neural networks." In 2016 15th IEEE International Conference on Machine Learning and Applications (ICMLA), pp. 61-68. IEEE, 2016.

[27] Suárez, Patricia L., Angel D. Sappa, and Boris X. Vintimilla. "Infrared image colorization based on a triplet dcgan architecture." In Proceedings of the IEEE Conference on Computer Vision and Pattern Recognition Workshops, pp. 18-23. 2017.

[28] Chen, Dongdong, Jing Liao, Lu Yuan, Nenghai Yu, and Gang Hua. "Coherent online video style transfer." In Proceedings of the IEEE International Conference on Computer Vision, pp. 1105-1114. 2017.

[29] Chen, Dongdong, Lu Yuan, Jing Liao, Nenghai Yu, and Gang Hua. "Stereoscopic neural style transfer." In Proceedings of the IEEE Conference on Computer Vision and Pattern Recognition, pp. 6654-6663. 2018.

[30] Chen, Dongdong, Lu Yuan, Jing Liao, Nenghai Yu, and Gang Hua. "Stylebank: An explicit representation for neural image style transfer." In Proceedings of the IEEE conference on computer vision and pattern recognition, pp. 1897-1906. 2017.

[31] SENSIAC. 2008. Military Sensing Information Analysis Center. Retrieved from <https://blogs.upm.es/gti-work/2013/05/06/sensiac-dataset-for-automatic-target-recognition-in-infrared-imagery/>

[32] Data available at <https://ieee-dataport.org/open-access/thermal-visual-paired-dataset>

[33] Liu, Shuo, Mingliang Gao, Vijay John, Zheng Liu, and Erik Blasch. "Deep Learning Thermal Image Translation for Night Vision Perception." ACM Transactions on Intelligent Systems and Technology (TIST) 12, no. 1 (2020): 1-18.

[34] Tao, Dan, Junsheng Shi, and Feiyan Cheng. "Intelligent Colorization for Thermal Infrared Image Based on CNN." In 2020 IEEE International Conference on Information Technology, Big Data and Artificial Intelligence (ICIBA), vol. 1, pp. 1184-1190. IEEE, 2020.

[35] Woo, Jonghye, Maureen Stone, and Jerry L. Prince. "Multimodal registration via mutual information incorporating geometric and spatial context." IEEE Transactions on Image Processing 24, no. 2 (2014): 757-769.

[36] Zhu, Jun-Yan, Taesung Park, Phillip Isola, and Alexei A. Efros. "Unpaired image-to-image translation using cycle-consistent adversarial networks." In Proceedings of the IEEE international conference on computer vision, pp. 2223-2232. 2017.

[37] Wang, Zhongling, Zhenzhong Chen, and Feng Wu. "Thermal to visible facial image translation using generative adversarial networks." IEEE Signal Processing Letters 25, no. 8 (2018): 1161-1165.

[38] Lin, Chih-Lung, and Kuo-Chin Fan. "Biometric verification using thermal images of palm-dorsa vein patterns." IEEE Transactions on Circuits and systems for Video Technology 14, no. 2 (2004): 199-213.

[39] Jeong, Mira, Byoung Chul Ko, and Jae-Yeal Nam. "Early detection of sudden pedestrian crossing for safe driving during summer nights." IEEE Transactions on Circuits and Systems for Video Technology 27, no. 6 (2016): 1368-1380.

[40] Zhang, Teng, Arnold Wiliem, Siqi Yang, and Brian Lovell. "Tv-gan: Generative adversarial network based thermal to visible face recognition." In 2018 international conference on biometrics (ICB), pp. 174-181. IEEE, 2018.

[41] Yang, Sen, Bin Luo, Chenglong Li, Guizhao Wang, and Jin Tang. "Fast grayscale-thermal foreground detection with collaborative low-rank decomposition." IEEE Transactions on Circuits and Systems for Video Technology 28, no. 10 (2017): 2574-2585.

[42] Fonaryov, Mark, and Michael Lindenbaum. "On the Minimal Recognizable Image Patch." In 2020 25th International Conference on Pattern Recognition (ICPR), pp. 6734-6741. IEEE, 2021.

[43] Kingma, Diederik P., and Jimmy Ba. "Adam: A method for stochastic optimization." arXiv preprint arXiv:1412.6980 (2014).

[44] Zuo, Ling-Qun, Hong-Mei Sun, Qi-Chao Mao, Rong Qi, and Rui-Sheng Jia. "Natural scene text recognition based on encoder-decoder framework." IEEE Access 7 (2019): 62616-62623.

[45] Goswami, Suranjan, and Satish Kumar Singh. "A simple deep learning based image illumination correction method for paintings." Pattern Recognition Letters 138 (2020): 392-396.

[46] Ji, Donghong, Peng Tao, Hao Fei, and Yafeng Ren. "An end-to-end joint model for evidence information extraction from court record document." Information Processing & Management 57, no. 6 (2020): 102305.

[47] Nayak, Tapas, and Hwee Tou Ng. "Effective modeling of encoder-decoder architecture for joint entity and relation extraction." In Proceedings of the AAAI Conference on Artificial Intelligence, vol. 34, no. 05, pp. 8528-8535. 2020.

[48] Ly, Nam Tuan, Cuong Tuan Nguyen, and Masaki Nakagawa. "An attention-based row-column encoder-decoder model for text recognition in Japanese historical documents." Pattern Recognition Letters 136 (2020): 134-141.

Du, Xianzhi, Tsung-Yi Lin, Pengchong Jin, Golnaz Ghiasi, Mingxing Tan, Yin Cui, Quoc V. Le, and Xiaodan Song. "SpineNet: Learning scale-permuted backbone for recognition and localization." In Proceedings of the IEEE/CVF conference on computer vision and pattern recognition, pp. 11592-11601. 2020.